Biomedicine & Pharmacotherapy 194 (2026) 118930

Contents lists available at ScienceDirect

Biomedicine & Pharmacotherapy

journal homepage: www.elsevier.com/locate/biopha

Targeting tumors and inflammation: A quinoline–chalcone ruthenium complex with therapeutic promise

Kateřina Veselá [a,b], Ameneh Tatar [a,b], Zdeněk Kejík [a,b], Nikita Abramenko [a], Jan Čejka [c], Robert Kaplánek [a], Michal Masařík [a,d,e], Petr Babula [d,e], Pavel Martásek [b,*], Milan Jakubek [a,b,**]

[a] BIOCEV, First Faculty of Medicine, Charles University, Průmyslová 595, Vestec, 252 50, Czech Republic
[b] Department of Paediatrics and Inherited Metabolic Disorders, First Faculty of Medicine, Charles University and General University Hospital in Prague, Prague, Czech Republic
[c] Department of Solid State Chemistry, Institute of Chemical Technology, Technická 5, Prague 166 28, Czech Republic
[d] Department of Pathological Physiology, Faculty of Medicine, Masaryk University, Kamenice 5, Brno 625 00, Czech Republic
[e] Department of Physiology, Faculty of Medicine, Masaryk University, Kamenice 5, Brno 625 00, Czech Republic

ARTICLE INFO

Keywords:
Ru-complex
Quinoline
Chalcone
Anti-inflammatory
Anticancer
Head and neck carcinoma

ABSTRACT

Head and neck cancers remain among the most challenging malignancies to treat and are often linked to lifestyle-related risk factors such as smoking and alcohol consumption. These factors not only initiate tumor development but also promote chronic inflammation and activate key oncogenic pathways, including NF-κB signaling and pro-angiogenic cytokines IL-6 and IL-8. Research into emerging therapeutic approaches has identified metal-based compounds—especially ruthenium(II) complexes—as promising alternatives to traditional platinum-based drugs. In this study, we report the design, synthesis and X-RAY characterization of a ruthenium(II) complex incorporating a quinoline-chalcone hybrid ligand, designed for enhanced anticancer and anti-inflammatory potential. The resulting compound, referred to as complex 2, demonstrated significant activity against HPV-negative head and neck cancer cell lines. It exhibited strong cytostatic, antiproliferative, and migrastatic effects, along marked suppression of NF-κB activation and a notable decrease in IL-6 and IL-8 levels due to direct interactions. These findings highlight complex 2 as a promising multitarget agent capable of targeting both tumor progression and the inflammatory microenvironment. Overall, complex **2** is a potential candidate for combination therapies targeting head and neck cancer.

1. Introduction

Head and Neck Squamous Cell Carcinoma (HNSCC) includes a wide group of difficult-to-treat tumors, including tumors from the nasal and oral cavity to the larynx. HNSCC tumors are primarily caused by tobacco and alcohol consumption (HPV-) or human papillomavirus (HPV+), especially HPV-16 [1–3]. During the development of HNSCC, when genetic and epigenetic alterations, leading to the inactivation of tumor suppressors and activation of proto-oncogenes [4–6]. It is chronic exposure to cigarette smoke that causes inflammation, which stimulates activation of nuclear factor kappa B (NF-κB) signaling, leading to a subsequent increase in pro-angiogenic cytokines such as interleukin 6 (IL-6) and interleukin 8 (IL-8), and consequently to the development of HNSCC [7,8]. Conversely, the repression of NF-κB activity and IL-6/IL-8 signaling displays promising therapeutic potential against HNSCC [9,10].

The development of metal-based anticancer agents has led to significant advancements in medicinal chemistry, with ruthenium(II) arene complexes emerging as promising alternatives to traditional platinum-based drugs [11]. These complexes offer several advantages such as tunable ligand environments, lower toxicity, and the ability to interact selectively with biological targets [12,13]. Half-sandwich arene Ru(II) organometallic complexes are emerging as promising candidates in biomedical research. These compounds typically consist of a stable arene, a reactive chloride for biomolecular interaction, and a bioactive ligand, which structure can be modified to fine-tune therapeutic

* Corresponding author.
** Corresponding author at: BIOCEV, First Faculty of Medicine, Charles University, Průmyslová 595, Vestec, 252 50, Czech Republic.
E-mail addresses: pavel.martasek@lf1.cuni.cz (P. Martásek), Milan.Jakubek@lf1.cuni.cz (M. Jakubek).

https://doi.org/10.1016/j.biopha.2025.118930
Received 19 September 2025; Received in revised form 5 December 2025; Accepted 16 December 2025
Available online 19 December 2025

potential [13–15]. Although Ru-complexes have not been widely studied against HNSCC, a few studies suggest the promising potential of Ru (II)-complexes against head and neck cancer (HNC) [16–18]. Guo et al. found that a Ru(II)-complex inhibited the growth of human esophageal cancer cell line EC109 at low concentrations [16]. Santi et al. reported, that Ru(II) displayed promising strong cytostatic effect in an HPV+ HNSCC 3D *in vitro* model [19]. It should also be mentioned that Ru(II)-complexes are starting to be studied as migrastatic agents [20].

Chalcones, featuring an α,β-unsaturated ketone moiety, are versatile scaffolds with a broad spectrum of effects, including antioxidant, antibacterial, anti-inflammatory, and anticancer properties [21]. Their simple core structure allows for easy modification, particularly through the introduction of heteroaryl groups on one aromatic ring to enhance functionality or enable metal coordination. One such modification involves incorporating quinoline into one side of the chalcone structure [22]. Quinoline and its derivatives, especially 8-hydroxyquinoline, are well-recognized for both their pharmacological strength and their capacity to bind metal ions [23,24]. These compounds have shown promise across multiple therapeutic areas, such as anticancer, antimicrobial, antiviral, and neuroprotective effects [25–28]. Numerous high-impact studies suggest that their anticancer effects in various cancer models are deeply associated with NF-κB targeting [29]. In the case of oral squamous cell carcinoma (OSCC), the antitumor effect of butein is linked to the repression of NF-κB signaling.

The integration of ruthenium, chalcone, and quinoline into a single molecular framework presents a compelling strategy for developing novel anticancer agents. In this study, we present the synthesis and characterization of a Ru(II) arene complex incorporating a quinoline-functionalized chalcone ligand. Specifically, the design features an 8-hydroxyquinoline group on one end of the chalcone for metal coordination and a 3,4,5-trimethoxyphenyl moiety on the other to enhance biological effectiveness. We investigated the cytotoxic and migrastatic effect of complex **2** using standard assays (MTT, CFA, wound healing assay). These effects were investigated in HNC cell lines, both HPV+ (Hep-2, KB) and HPV- (CAL 27, SCC-9, Detroit 562, FaDu and TR146). Complex **2** proved to be more effective in HPV- lines. Furthermore, the anti-inflammatory effect of complex **2** was investigated. Complex **2** showed effects on both NF-κB and the cytokines IL-6 and IL-8. Since the effect of complex **2** on interleukin 6 receptor (IL-6R) was minimal, it can be assumed that there is a direct effect of complex **2** on IL-6, or it can be assumed that the level of IL-6 may also be affected by decrease in the level of NF-κB. This structure aims to take advantage of the combined effects of these components to produce a compound with potent anti-migratory and anti-inflammatory properties in HNC models.

2. Materials and methods

2.1. Materials for synthesis

All reagents were purchased from commercial suppliers and used as received, without further purification. Silica gel (32–63 μm, 60 Å) was used for the purification of the synthesized compounds. NMR spectra were recorded on a 400 MHz instrument (JEOL, Tokyo, Japan) at 25°C. Chemical shifts (δ) are reported in ppm and coupling constants (J) in Hz. The ^{1}H and ^{13}C chemical shifts are referenced to TMS, using the solvent signals (DMSO-*d6* 2.50 ppm, DMSO-*d6* 39.52 ppm). NMR data processing was carried out with MestReNova software (Mestrelab Research S.L., version 14.2.1). Mass spectrometry data were obtained in positive mode electrospray ionization (ESI^{+}) using a high-resolution hybrid Ion Trap-Orbitrap mass spectrometer (LTQ Orbitrap Velos, Thermo Scientific). An HPLC system (LCMS-2020, Shimadzu, Japan) was used to determine the purity of the synthesized compounds. Separation was performed using a gradient method on a C18 column, with acetonitrile and Milli-Q water acidified with 0.1 % (v/v) formic acid as the mobile phase. For NMR spectra of all products, please refer to the Supplementary Information.

2.2. Synthesis

Preparation of compound 1: To a solution of 3′,4′,5′-trimethoxyacetophenone (210 mg, 1 mmol) in ethanol (10 mL), $LiOH{\cdot}H_2O$ (82 mg, 2 mmol) was added, followed by the addition of 8-hydroxyquinoline-2-carbaldehyde (173 mg, 1 mmol). The reaction mixture was stirred at room temperature and allowed to proceed overnight. Reaction progress was monitored by TLC (DCM:MeOH, 99:5 v/v). Upon completion, 1 M aqueous HCl was added dropwise until the pH reached neutral. The resulting precipitate was collected by filtration, washed with water, and dried to afford the desired product (194 mg, 53 %). ^{1}H NMR (400 MHz, DMSO-d_6) δ: 9.85 (S, 1 H), 8.57 (d, J = 15.6 Hz, 1 H), 8.41 (d, J = 8.5 Hz, 1 H), 8.13 (d, J = 8.5 Hz, 1 H), 7.92 (d, J = 15.4 Hz, 1 H), 7.51 (s, 2 H), 7.49 (d, J = 7.8 Hz, 1 H), 7.43 (d, J = 8.2 Hz, 1 H), 7.14 (d, J = 8.9 Hz, 1 H), 3.93 (s, 6 H), 3.80 (s, 3 H). ^{13}C NMR (101 MHz, DMSO-d_6) δ: 188.3, 153.5, 153.0, 151.3, 142.9, 142.4, 138.3, 136.8, 132.7, 128.6, 126.8, 122.1, 117.6, 111.6, 106.6, 60.2, 56.3. MS (ESI): for $C_{21}H_{19}NO_5$ calcd. $[M+H]^{+}$ 366, found: 366.

Preparation of Ru-complex 2: Dichloro(p-cymene)ruthenium dimer (33 mg, 0.05 mmol) and compound **1** (20 mg, 0.05 mmol) were added in 20 mL of chloroform, and the mixture was refluxed for 24 h. The starting materials were consumed, and a solid product formed. The solvent was then removed under reduced pressure, and the product was recrystallized from a hexane-dichloromethane mixture to yield complex **2**. To remove trace impurities, the solid was further purified by column chromatography using a methanol:DCM (5:95, v/v) elution, resulting in pure complex **2** (15 mg, 47 %). ^{1}H NMR (400 MHz, DMSO-d_6) δ 8.57 (d, J = 15.7 Hz, 1 H), 8.36 (d, J = 8.5 Hz, 1 H), 8.33 (d, J = 8.5 Hz, 1 H), 8.28 (d, J = 15.8 Hz, 1 H), 7.59 (s, 2 H), 7.32 (t, J = 7.9 Hz, 1 H), 6.86 (dd, J = 7.9, 1.1 Hz, 1 H), 6.78 (dd, J = 8.0, 1.1 Hz, 1 H), 5.91 (d, J = 5.8 Hz, 1 H), 5.68 (d, J = 6.0 Hz, 1 H), 5.63 (d, J = 5.9 Hz, 1 H), 5.44 (d, J = 6.1 Hz, 1 H), 3.96 (s, 6 H), 3.81 (s, 3 H), 2.42 (p, J = 6.9 Hz, 1 H), 2.25 (s, 3 H), 0.95 (d, J = 6.9 Hz, 3 H), 0.81 (d, J = 6.9 Hz, 3 H). ^{13}C NMR (101 MHz, DMSO-d_6) δ: 188.2, 169.5, 153.1, 152.6, 144.6, 144.2, 142.6, 137.3, 132.4, 130.3, 129.2, 126.2, 121.0, 114.2, 109.5, 106.7, 101.4, 99.6, 87.0, 80.8, 79.9, 78.7, 60.3, 56.4, 54.9, 30.3, 21.8, 21.5, 18.5. HRMS (ESI): for $C_{31}H_{32}N_1O_5Ru$ calcd. $[M-Cl]^{+}$ 600.13185, found: 600.13219.

2.3. Cell lines

For *in vitro* cell assays were used HPV- cell lines (CAL 27, SCC-9, Detroit 562, FaDu, TR146) and HPV+ cell lines (Hep-2, KB). HGF was used as a control cell line. THP1-Blue NF-κB Monocytes were used to determine NF-κB activity. For more information about cell lines and handling information, see Supplementary materials.

2.4. Docking studies of IL-6 (IL-6R), NF-kB and IL-8 with complex 2

The 3D crystal structures of the target proteins (IL-6, IL-6R, IL-8 and NF-κB) were retrieved from the Protein Data Bank database with PDB IDs 1P9M (for crystal structure of the human IL-6/IL-6R complex), 1ALU (human IL-6 monomer), 3IL8 (human IL-8 dimer) and 1NFI (human NF-κB:IκB complex) [30]. Dimeric or multimeric forms were generated when required. Similarly, the coordinates of a p50-p65 NF-κB dimer were obtained by removing the coordinates corresponding to IκB with COOT [31].

The obtained structures underwent a preparation process prior to performing docking. This process involved the removal of all bound water molecules, ligands that were used for performing of the docking studies according to protocols from AutoDock Vina software [32]. In the structures obtained from the PDB database, all bound water molecules and ligands were removed and saved using the UCSF ChimeraX software, as pdb files [33]. The 3D structures of tested compound (complex

2) were generated using 3D ChemDraw software. All structural models were energy-minimized using YASARA [34].

Molecular docking was performed with AutoDock Vina software. The interactions between receptors with tested ligands were visualized and analyzed using PyMOL, UCSF ChimeraX and BIOVIA Discovery Studio Visualizer. The interaction diagrams and 3D representations of the protein–ligand complexes were generated with BIOVIA DSV and ChimeraX, respectively [33,35,36].

For the docking of the complex **2**, "sequential" molecular docking was performed because the software from the AutoDock Vina suite is unable to cope with the η^6 arene coordination of ruthenium. Hence, an organic fragment lacking the benzyl ring system was first docked to the target protein (with ruthenium substituted by phosphorus for the calculations). The complex with this bound fragment is then used as the target for targeted docking the benzyl ring fragment. The binding free energies of the docked complex **2** ligands are obtained with the PRODIGY server [37].

2.5. MTT viability assay

A colorimetric MTT cell metabolic activity assay was used to determine the cytotoxicity of complex **2**. The cells (mentioned above) were cultured under standard conditions. Cells were plated in 96-well plates at density of 10 000 cells per well (200 μL) and grown for 24 h. Medium was then replaced with medium containing complex **2** in the concentration series (from 0 μM to 200 μM) and were cultured another 24 h, 48 h and 72 h. Afterwards, the medium was exchanged for the MTT solution, yellow tetrazolium dye (3-(4,5-dimethylthiazol-2-yl)-2,5-diphenyltetrazolium bromide (Sigma-Aldrich, Merck, Germany) and incubated for 2 h at 37 °C. After that, the yellow tetrazole dye was removed, and DMSO was used to dissolve the reduced purple formazan formed in living cells, which was then shaken for 30 s. The absorbance of the converted dye was measured at a wavelength of 570 nm using an INFINITE 200 PRO microplate reader (TECAN, Switzerland). Experiment was performed in quadruplicates and repeated three times.

The cell inhibitory concentration (IC) was calculated using the equation IC = ($A_{complex\ 2}$ well/mean $A_{control}$ wells) × 100 %. The half-maximal inhibitory concentration (IC_{50}) was calculated from dose–response curves using GraphPad Prism 10 (GraphPad Software, Inc., La Jolla, CA, USA). The selectivity index towards cancer cells were calculated as a ration of the average of the IC_{50} value for HGF and the IC_{50} value for the corresponding cancer cell line.

2.6. Colony formation assay

Cells were plated in 6-well plates at a density 100 000 cells per well (10 000 cells / 200 μL) and grown for 24 h. The medium was then replaced with medium containing complex **2** at the concentration of IC_{50} and were cultured another 24 h. Afterwards cells were re-plated in new 6-well plates at density 500 cells per well and grown approximately 2 weeks. The cell culture media was replaced every 2–3 days. When a visible colony appeared in the 6-well plates, the culture was terminated, and the cells were washed twice with ice-cold PBS. Next, the cells were fixed with ice-cold methanol for 10 min and stained with 0.5 % crystal violet solution for 30 min at room temperature. The experiment was performed in four independent replicates.

2.7. Wound healing assay

The wound healing activity of complex **2** was detected by using the ibidi culture-insert 2 well in a μ-dish. Cells were plated by applying 70 μl of the cell suspension at density 50 000 cells into both wells of the culture-insert 2 well and grown during the weekend. When the confluency was achieved, sterile tweezers were used to detach the culture-inserts 2 well from the μ-dish. The cell layer was then gently washed with PBS. Cell layer was treated with medium containing complex **2** at the concentration of IC_{25} and after that, the wound closure was observed and photographed by inverted light microscope (0 – 55 h of incubation). The experiment was performed in four independent replicates.

2.8. NF-κB activity assay + MTT viability assay

THP1-Blue NF-κB Cells, NF-κB SEAP Reporter Monocytes (InvivoGen, USA) were determined after 20–24 h of incubation according to the manufacturer's protocol. Briefly, 1×10^6 cells/mL in RPMI were seeded in 96-well plates (180 μL) and treated and incubated with complex **2**, LPS (10 ng/mL) (LPS-EB, O111:B4, InvivoGen, USA) or both overnight at 37°C, 5 % CO_2 in a total volume of 200 μL. The following day, the activation of NF-κB was analyzed as the secretion of embryonic alkaline phosphatase (SEAP). The supernatant (20 μL) from the cells was transferred to 96-well plates, and 180 μL of Quanti-Blue was added. The plates were incubated for 2 h at 37 °C, and the absorbance was measured at 600 nm in an INFINITE 200 PRO microplate reader (TECAN, Switzerland).

It was added 20 μL of sterile filtered MTT (3-(4,5-dimethylthiazolyl)-2,5-diphenyltetrazolium bromide; Sigma-Aldrich, Merck, Germany) solution (5 mg/mL in PBS) to the remaining overnight culture of THP1-Blue NF-κB Cells from the above NF-κB activity assay in 96-well plates, which were incubated at 37 °C (see above). After 2 h of incubation at 37°C, the supernatant was removed and dissolved the blue formazan product generated in cells by the addition of 100 μL of DMSO in each well. The plates were then gently shaken for 30 s at room temperature to dissolve the precipitates. The absorbance was measured at 570 nm in an INFINITE 200 PRO microplate reader (TECAN, Switzerland) [38].

2.9. Determination of intracellular p65-NF-κB

To determine NF-κB p65 Transcription Factor by ELISA, Assay Kit was used (Abcam, ab133112). After the treatment of cells (THP1-Blue NF-κB Cells) with complex **2** and LPS (10 ng/mL), and with just LPS (10 ng/mL) cells were lysed with RIPA Lysis and Extraction (Thermo Scientific) and centrifuged at 1500 g for 10 min, supernatants were collected and used for the determination of intracellular p65- NF-κB by ELISA. In this assay, a specific double-stranded DNA (dsDNA) sequence containing the NF-κB p65 response element is immobilized onto the wells of a 96-well plate. NF-κB p65 present in the sample binds specifically to these response elements. Bound p65 is subsequently detected using a primary antibody specific for NF-κB p65, followed by a horseradish peroxidase (HRP)-conjugated secondary antibody. The relevant background values were subtracted from the measured values. Absorbance was measured at 450 nm using an INFINITE 200 PRO microplate reader (Tecan, Switzerland).

2.10. IKKβ inhibition assay

IKKβ inhibition was determined using the IKKβ Kinase Assay Kit (BPS Bioscience, USA). IKKβ activity was measured in the presence of complex **2** (5, 10, and 20 μM) according to the manufacturer's protocol. Kinase-Glo® MAX (Promega, #V6071) was used as the detection reagent, with an incubation time of 15 min. Blank values were subtracted from all measurements. Luminescence was measured with an integration time of 1 s using a Spark microplate reader (Tecan, Switzerland).

2.11. ELISA assay (IL-6/IL-6R/IL-8)

Human ELISA Kit (IL-6/IL-6R/IL-8) (Sigma-Aldrich, Merck, Germany) was used for quantitative detection of human IL-6/IL-6R/IL-8 after treatment with complex **2**. Specific antibody is coated on a 96-well plate. Standards and samples (containing complex **2** and IL-6 or IL-6R or IL-8 standard) are pipetted into the appropriate wells and IL-6/IL-6R/IL-8 in the sample is bound to the wells by the immobilized

antibody. Concentration 500 pg/mL of IL-6/IL-6R/IL-8 was used. Positive control samples contained just IL-6/ IL-6R/IL-8 standard (Pepro-Tech, ThermoFisher scientific, USA). Samples were treated with complex **2** at concentrations of 5, 10 and 20 μM and also 500 pg/mL of IL-6/IL-6R/IL-8. Then the wells were washed and biotinylated anti-human antibody was added. After another washing steps, HRP-conjugated streptavidin was pipetted to the wells. After the final washing, TMB substrate solution was added to the wells until color developed, based on the amount of IL-6/IL-6R/IL-8 bound. The stop solution was added, and changing color was observed. Intensity of the color was measured at 450 nm in an INFINITE 200 PRO microplate reader (TECAN, Switzerland).

2.12. MicroScale thermophoresis

To investigate the interaction between complex **2** and IL-6, IL-8, and IL-6R, microscale thermophoresis (MST) was performed. His-tagged interleukins (ACROBiosystems, Switzerland) were used. The Monolith His-Tag Labeling Kit RED-tris-NTA 2nd Generation (Cat# MO-L018) was employed to label the His-tagged interleukins with the RED-tris-NTA 2nd Generation dye. A mixture of 90 μL of IL-6, IL-8, or IL-6R (200 nM) and 90 μL of dye (100 nM) was prepared and incubated for 30 min. The labeled interleukins were then used for the binding assay. For the MST titration series, 10 μL of PBS-T (1 ×) was added to wells 2–16. Complex **2** (20 μM; yielding a final concentration of 200 μM in well 1) was added to well 1. Subsequently, 10 μL was transferred from well 1 to well 2 and mixed. The serial dilution was continued by transferring 10 μL from each well to the next (wells 2–16), with mixing after each transfer. The final 10 μL from well 16 was discarded. Next, 10 μL of the labeled protein was added to each well (1–16) and mixed thoroughly. The final concentration of the labeled target protein in each well was 50 nM. Capillaries were then loaded, and measurements were performed at 60 % LED power and 60 % or 80 % MST power (Monolith NT.115). The dissociation constant (Kd) was determined using the Kd fit in MO.Affinity Analysis.

2.13. Statistical analysis

The graphs of colony formation assay (CFA), MA, IL-6, IL-6R, IL-8 and NF-κB activity are presented as the mean ± SEM from at least three independent experiments. Differences in these assays were assessed using one-way ANOVA with Dunnett's multiple comparison test. All data were analyzed using GraphPad Prism 10 (GraphPad Software, Inc., La Jolla, CA, USA). Additionally, p-values less than 0.05 were considered to be statistically significant (ns= not significant, * $p < 0.05$, ** $p < 0.01$, *** $p < 0.001$, and **** $p < 0.0001$).

3. Results

3.1. Preparation of quinoline-ruthenium complex

The synthetic route to the quinoline framework is outlined in Scheme 1. The ligands were synthesized through a Claisen–Schmidt condensation between 8-hydroxyquinoline-2-carbaldehyde and 3′,4′,5′-trimethoxyacetophenone. The resulting ligand was isolated in reasonable yields (53 %) as a pale-yellow solid. The Ru(II) complexes were synthesized by reacting dichloro(p-cymene)ruthenium dimer with the ligand in chloroform under reflux conditions, resulting in a reddish solid, which was purified by column chromatography (yield 47 %). The purity of the compounds was analyzed using HPLC and was found to be over 95 %. The complex was characterized using X-ray diffraction, NMR spectrometry, and high-resolution mass spectrometry (HR-MS). The ^{1}H NMR spectra of the complexes exhibit typical signals for the isopropyl group protons of p-cymene, including two sets of doublets for methyl protons (CH-(C<u>H</u>$_3$)$_2$) around 0.8–0.9 ppm, a septet at 2.42 ppm for the methylene protons (C<u>H</u>-(CH$_3$)$_2$). Additionally, four sets of doublets corresponding to the aromatic protons of (p-cymene)ruthenium appear in the range of 5.5–5.9 ppm and protons of methyl group at 2.25 ppm. The aromatic protons of the quinoline ligands are observed between 7.3 and 10 ppm, while two resolved singlets signals at 3.8 ppm and at 3.96 ppm with an integral ratio of 1:2 correspond to the methoxy groups on the quinoline.

3.2. X-RAY

Single crystals suitable for X-ray diffraction analysis of complex **2** were obtained by slow diffusion chloroform of into a small amount of DMSO. The crystal structures were determined by single-crystal X-ray diffraction, and perspective drawings of the complexes are shown in Fig. 1. Complex **2**, $C_{31}H_{32}ClNO_5Ru$, $M = 635.12$ g.mol^{-1}, monoclinic system, space group P-1, $a = 10.3624(7)$ Å, $b = 11.1778(8)$ Å, $c = 21.0589(3)$ Å, $\alpha = 80.859(3)°$, $\beta = 73.752(2)°$, $\gamma = 71.317(2)°$, $Z = 4$, $V = 1385.75(17)$ Å^3, $D_c = 1.522$ g.cm^{-3}, μ(Cu-Kα) $= 3.911$ mm^{-1}, block-like crystal dimensions of 0.11 × 0.14 × 0.21 mm. Diffraction patterns of the complex **2** single - crystal were collected at 100(1) K using a Bruker D8 Venture diffractometer equipped with a MetalJet D2 X-ray source (Excillum,gallium Kα), a 4-circle goniometer and a Photon III detector. The structure was solved by direct methods [39] and

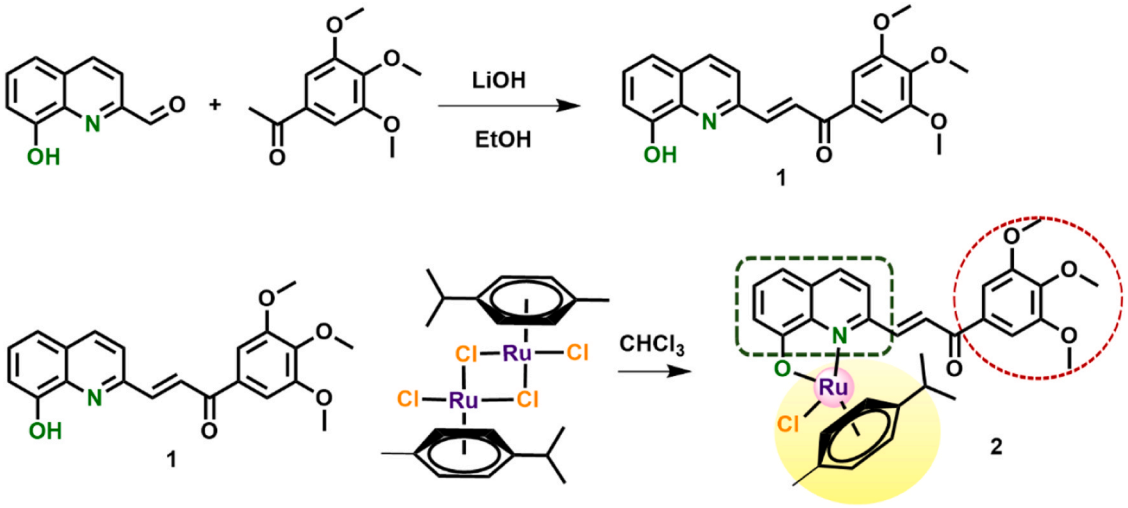

Scheme 1. Preparation of quinoline- chalcone-ruthenium complex.

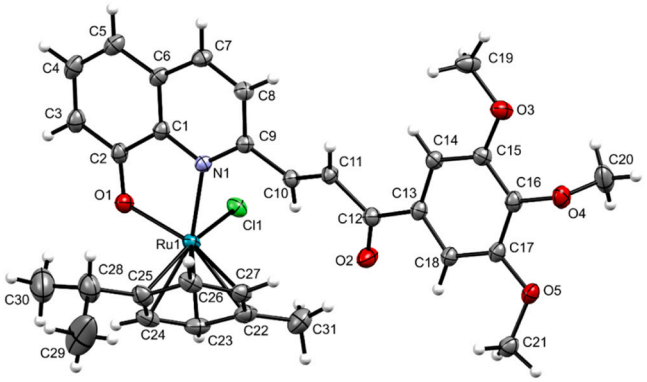

Fig. 1. ORTEP drawing of complex **2**, ellipsoids displayed at 50 % probability level.

anisotropically refined by full matrix least squares on F squared using the CRYSTALS suite of programs [40] to the final values $R_1 = 0.046$ (7606 observed reflections) and $wR = 0.123$ using 7812 independent reflections ($\Theta_{max} = 73.3°$), 363 parameters and 1 restraints. The hydrogen atoms were placed in calculated positions and refined with riding constraints [41]. The disordered prop-2-yl group positions were found in difference electron density maps and refined with restrained geometry, the occupancy ratio of the major to the minor part was 722/278. The occupancy was refined constrained to full. The structure was deposited into Cambridge Structural Database under number CCDC 2463777.

3.3. Docking studies of IL-6, NF-κB and IL-8 with complex 2

Table 1 summarizes the predicted binding energies calculated for complex **2** toward selected protein targets. Based on the calculations, the complex **2** ligand shows the highest affinity for the IL-6 dimer (IL-6d) with a value of −12.71 kcal/mol, the binding affinity for IL-6R (see Table S2 and Figure S7 in ESI) was also calculated and was slightly lower than the affinity for IL-6d, at −10.50 kcal/mol, suggesting that the complex **2** ligand interacts with the dimeric form of IL-6 rather than its receptor. Calculations further showed that the ligand also exhibited significant affinity for NF-kB and IL-8d (−9.70 and −8.49 kcal/mol, respectively).

To compare the results, the same calculations were performed with compound **1** (Scheme 1) to clarify the extent of the Ru(II) moiety's effect on binding ability. The results suggest that the presence of Ru(II) has a significant effect on the binding affinity, consequently, the properties of complex **2**.

Fig. 2 illustrates the placement of the ligand (complex **2**) on the surface of the IL-6d. In this docking pose, stabilization is achieved through multiple interactions. Strong conventional hydrogen bonds between ASN B:144 (via oxygen from trimethoxyphenyl group) and LYS B:120 (with carbonyl group). Additionally, carbon hydrogen bonds involving PRO B:139, GLU B:99, PRO A:141, and GLU A:99 which interact with the methyl groups of the trimethoxyphenyl moiety, further enhance stability. π-anion interactions between GLU A:99 and GLU B:99 with the benzene ring of the trimethoxyphenyl moiety also contribute

Table 1
Results of predicted binding energies of complex **2** and compound **1** with target proteins.

Receptor	Binding Energy (kcal/mol)	
	Complex 2	Compound 1
IL-6d	-12.71	-7.57
NF-κB	-9.7	-8.73
IL-8d	-8.49	-7.49

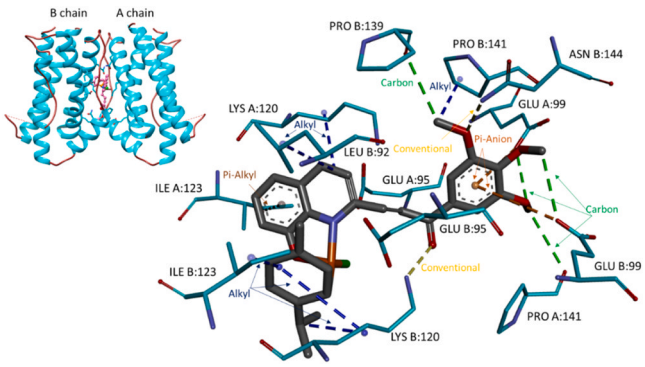

Fig. 2. Docking pose of complex **2** (colored magenta) in the dimeric form of IL-6 (binding energy −12.71 kcal/mol). The upper left inset provides a global view of the IL-6 dimer in cartoon representation (cyan helices and brown coils).

significantly to the binding. Moreover, hydrophobic residues like ILE A:123 forms π-alkyl interactions with the benzene ring of the quinoline moiety, while additional alkyl interactions are formed between ILE B:123 and LYS B:120 (via methylisopropyl benzene moiety), between LYS A:120 and LEU B:92 (via the pyridine ring of the quinoline moiety) and between PRO B:141 and methyl group from the trimethoxyphenyl moiety.

Fig. 3 illustrates the placement of the ligand (complex **2**) on the surface of the NF-κB protein. In this docking pose, stabilization is achieved through polar and hydrophobic interactions. Strong *conventional hydrogen bond*s between LYS C:221, GLN C:247 (via oxygens from trimethoxyphenyl group) and ARG C:246 (with carbonyl group). Additionally, *carbon hydrogen* bonds involving VAL C:244 and GLU C:222 with methyl groups of the trimethoxyphenyl moiety. Surrounding these polar contacts, hydrophobic packing further secures the ligand: *alkyl* interactions engage LYS C:221 (via methyl groups of the trimethoxyphenyl moiety), LYS C:218, VAL C:2448 and ARG C:246 via the pyridine ring of the quinoline moiety. Moreover, residues like LYS D:275 (with methylisopropyl benzene moiety), PHE D:310 (with methylisopropyl benzene moiety and with the pyridine ring of the quinoline moiety) and ARG D:308 (with benzene ring of the quinoline moiety) forms *π-alkyl* interactions.

Fig. 4 illustrates the placement of the ligand (complex **2**) on the surface of the IL-8d. The benzene ring of its quinoline moiety interacts with PHE A:17 through a *π–π stacking* interaction. *π–alkyl* contacts are observed between PHE A:21 and both the pyridine ring of the quinoline moiety and a methyl group from the trimethoxyphenyl moiety, as well as between LEU A:49 and the methylisopropyl benzene moiety. The same methylisopropyl benzene moiety also engages in a *π–anion* interaction

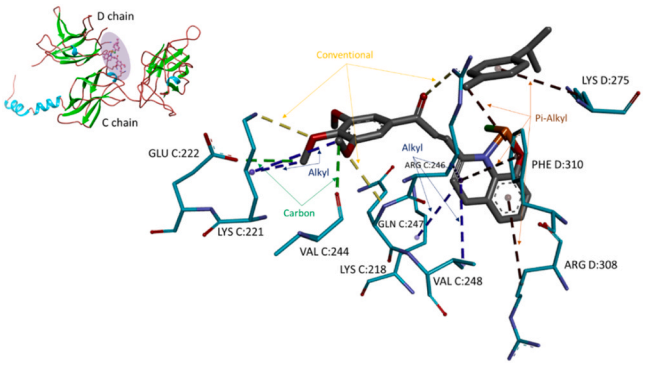

Fig. 3. Docking pose of complex **2** (colored magenta in violet area) on the surface of the NF-κB (binding energy −9.7 kcal/mol). The upper left inset provides a global view of the NF-κB in cartoon representation (cyan helices, brown coils and green strands).

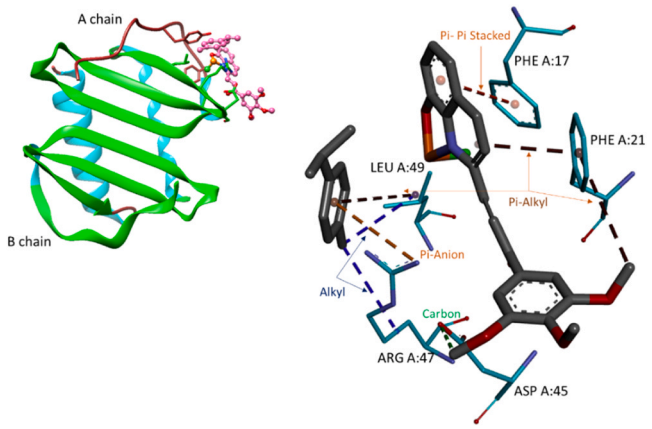

Fig. 4. Docking pose of complex **2** (colored magenta) in the dimeric form of IL-8 (binding energy −8.49 kcal/mol). Upper left inset provides a global view of the IL-8 in cartoon representation (cyan helices, brown coils and green strands).

with ARG A:47. Finally, ASP A:45 forms with methyl group from the trimethoxyphenyl moiety of the ligand *carbon hydrogen* bond.

3.4. Cytotoxic and migrastatic effect of complex 2 in vitro

We investigated the cytotoxic and migrastatic effect of complex **2** using standard assays (MTT, CFA, wound healing assay). These effects were investigated in HNC cell lines both HPV+ (Hep-2, KB) and HPV- (CAL 27, SCC-9, Detroit 562, FaDu and TR146), HGF was used as a control cell line. Testing revealed that complex **2** is more effective against HPV- cell lines both in regard to cytotoxicity and suppression of migration and invasiveness.

The cytotoxic activity of complex **2** was evaluated in normal (HGF) and cancer (CAL 27, SCC-9, Detroit 562, FaDu, TR146, Hep-2, KB) cells using the MTT viability assay. Cells were exposed to complex **2** in a concentration range of 0–200 μM under standard conditions in complete cell culture medium and cell viability was measured after 24 h, 48 h and 72 h of treatment. The average IC_{50} values after 24 h as well as a graphical representation of the selectivity index for all cell lines studied are shown in Fig. 5. The graphical representation of the IC_{50} values and their average values after 48 h and 72 h, including the selectivity index values, are shown in Figure S1 and Table S1, respectively.

Considering the results, it can be observed that complex **2** has the highest selectivity for the cell lines SCC-9 (OSCC, isolated from the tongue) and TR146 (buccal mucosa - metastatic line), for which it is the most toxic, at concentrations as low as of 6.0 μM (SCC-9) and 9.1 μM (TR146). In the case of the HPV+ cell lines Hep-2 and KB, complex **2** appears to be less cytotoxic, with IC_{50} values of 35.2 μM (Hep-2) and 20.15 μM (KB). Thus, in summary, complex **2** is more effective against HPV- cell lines compared to HPV+ lines in terms of cytotoxicity. The selectivity results also indicate that complex **2** is more selective for OSCC lines compared to other HNSCC lines.

The ability to form colonies after treatment with complex **2** was observed using CFA. Cells were exposed to complex **2** for 24 h at a concentration corresponding to the IC_{50} for the respective cell line, see Fig. 5. After re-plating, cells were incubated in complete cell culture medium for approximately 2 weeks under standard conditions and then stained with 0.5 % crystal violet solution and analyzed (Figure S2). A table showing the effect of clone formation along with a graphical representation can be seen in Fig. 6.

Although complex **2** is most toxic to SCC-9 and TR146 cell lines, it has the strongest effect on suppressing colony formation for cell lines CAL 27, Detroit 562, and FaDu. The efficiency of clone formation is only 15 % for the CAL 27 cell line, and for the Detroit 562 and FaDu cell lines, the efficiency of clone formation is less than 25 % in both cases. For the Hep-2 and KB HVP+ cell lines, the cloning efficiency is around 40 %. Even when CFA is used, complex **2** is more effective against HPV- cell lines.

To evaluate the effect of complex **2** on cell migration, an *in vitro* wound healing assay was performed. Using ImageJ software, the area at the cell monolayer border was determined. The enclosure of the bordered area was monitored over a period of 0–55 h. Table 2 shows the percentage of the area enclosed over time. Fig. 7 shows the graphical representation of wound area closure after 55 h and compare treated cells with the non-treated control, a graphical representation over time for a single cell line can be seen in Figure S4. Complex **2** inhibits cell migration most effectively in CAL 27 cell lines, where even after 55 h only 5 % area closure occurs, and FaDu, where after 48 h 19 % area closure occurs and after 55 h 32 % area closure occurs. In the case of the metastatic line TR146, there is 50 % area closure after 48 h, with no complete area closure even after 55 h. In the case of HPV+ cell lines, approximately 50 % area closure occurs after 48 h of treatment in the case of the KB line, but only 5 % area closure occurs after 55 h in the case of the Hep-2 line. Again, complex **2** is more effective against HPV- cell

Cell line	IC_{50} 24h [μM]
HGF	55.55
CAL 27	28.95
SCC-9	6.00
Detroit 562	15.65
FaDu	28.25
TR146	9.10
Hep-2	35.20
KB	20.15

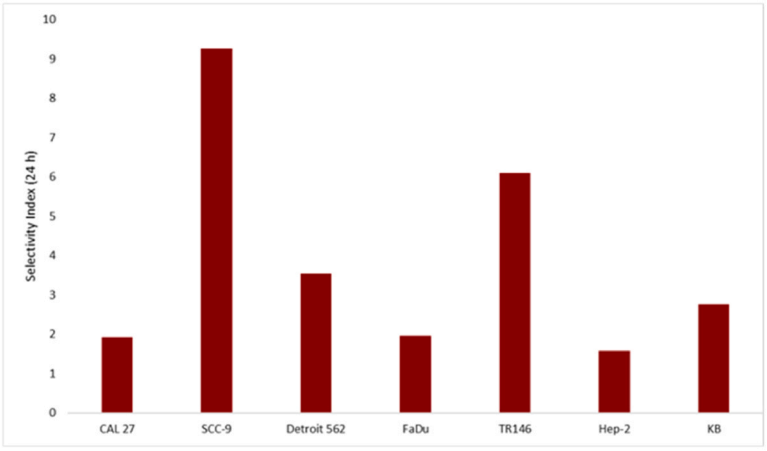

Fig. 5. Cytotoxic effect of complex **2**. MTT viable count assay was used to determine the cytotoxic effect. The IC_{50} values for cell lines (HGF, CAL 27, SCC-9, Detroit 562, FaDu, TR146, Hep-2 and KB) are shown in the table (left). The selectivity index (right) is determined for each cancer cell line against the healthy HGF cell line and was analyzed using the same assay.

Cloning efficiency (%) complex 2	
HGF	90
CAL 27	15
SCC-9	62
Detroit 562	22
TR146	53
FaDu	24
Hep-2	45
KB	42

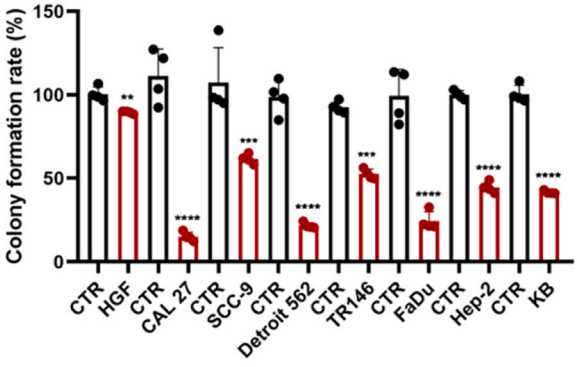

Fig. 6. Colony formation after 24 h treatment with complex **2** was analyzed using standard CFA. The concentration used corresponded to the resulting IC_{50} value. The effect of colony formation can be seen in the table (left). Colony formation rate is shown in graphical form compared to control (non-treated). Statistical analysis was performed using a one-way ANOVA with Dunnett's multiple comparison tests. Results are reported as **$p < 0.01$, ***$p < 0.001$, and ****$p < 0.0001$.

Table 2
Effect of complex **2** (**C2**) on cell migration in time (0 h, 24 h, 48 h and 55 h). Monitoring of area closure after treatment with complex **2** (the concentration corresponded to IC_{25}) compared to control (non-treated).

Wound area (%)																
	HGF		*CAL 27*		*SCC-9*		*Detroit 562*		*TR146*		*FaDu*		*Hep-2*		*KB*	
	CTR	*C2*	CTR	*C2*	CTR	*C2*	CTR	*C2*	CTR	*C2*	CTR	*C2*	CTR	*C2*	CTR	*C2*
0 h	0	0	0	0	0	0	0	0	0	0	0	0	0	0	0	0
24 h	22	15	23	3	61	32	54	15	58	21	43	7	54	3	67	23
48 h	65	24	56	4	100	57	100	57	100	50	78	19	95	4	90	46
55 h	97	72	83	5	100	91	100	82	100	75	100	32	100	5	100	57

lines.

Also, microscopic imaging of cell migration after 55 h of treatment can be seen in Fig. 8, in contrast with non-treated control cells. Additionally, microscopic images of cell migration after 24 h and 48 h can be seen in Figure S3. The entire progression of cell migration over time is recorded in a graphical curve with the deviations that can be seen in Figure S5. The monitored cell areas were stained after the completion of the observation period. The images of the stained cell areas are shown in Figure S6.

3.5. Anti-inflammatory activity of complex 2

We investigated the effect of complex **2** on LPS-induced NF-κB activation in THP1-Blue NF-κB cells (Fig. 9). This cell model carried gene for embryonic alkaline phosphatase under NF-κB controlled promoter. Complex **2** (concentrations of 5, 10 and 20 μM) inhibited LPS-induced expression of alkaline phosphatase. At a concentration of 20 μM, complex **2** showed a significant reduction of enzyme activity by up to approximately 70 %. However, a reduction of enzyme activity was also observed at a concentration of 5 μM, by approximately 20 %. Complex **2** did not show a significant cytotoxic effect on THP1-Blue NF-κB cells; therefore, it can be assumed that NF-κB activation was not due to cytotoxicity.

Above results strongly implies, that complex-**2** strongly decrease expression activity of NF-κB. Therefore, the effect of complex **2** on the DNA-binding activity of the transcription factor NF-κB (p65) s was evaluated following treatment with concentrations of 5, 10, and 25 μM, see Fig. 10. Even at the lowest concentration tested (5 μM), complex **2** caused an approximately 50 % reduction in NF-κB (p65) ability to bind to corresponding DNA sequence, indicating a substantial inhibitory effect. At higher concentrations, this effect was even more pronounced, treatment with 20 μM complex **2** resulted in the detection of less than 5 % of NF-κB (p65) bound to DNA.

IKKβ is a key protein responsible for the activation of NF-κB signaling [42,43]. To assess whether complex **2** affects this pathway, the kinase activity of IKKβ was measured following treatment (5–20 μM), see Fig. 11. As expected, complex **2** reduced IKKβ activity in a dose-dependent manner, with approximately 30 % inhibition observed at 5 μM. At a higher concentration of 20 μM, the activity of IKKβ was reduced by approximately 50 %. These results indicate that complex **2** can effectively interfere with NF-κB signaling, contributing to its overall anti-inflammatory and potential anti-cancer effects. It is well known, that, IKKβ promote degradation of IκBs (binding partner and repressor of p65). Furthermore, IKKβ participate in activation of p65 via its phosphorylation [42,43].

Furthermore, the effect of complex **2** on IL-6 was investigated using the IL-6 ELISA kit as a sandwich assay, see Fig. 12 (left). The obtained results suggest that complex **2** (at a concentration range of 5–20 μM) reduced IL-6 levels. The measured IL-6 concentration was reduced by approximately 30 % at a concentration of 20 μM of complex **2**. Even at a concentration of 5 μM, IL-6 concentration was reduced, but only by 15 %. The effect on IL-6R (Figure S8) was also investigated, showing a visible effect at a concentration of 20 μM, with approximately 10 % reduction.

The interaction with IL-8 was determined using the same procedure with a sandwich ELISA kit, see Fig. 12 (right). Again, the effect of complex **2** (at a concentration range of 5–20 μM) was determined. In the case of IL-8, complex **2** showed a significant effect. Complex **2** reduced the concentration of IL-8 by 35 % at 5 μM, and by about 45 % when 20 μM treatment of complex **2** was used.

As a proof of complex **2** binding to IL-6, IL-8 and IL-6R, we performed microscale thermophoresis (MST). We processed temperature jump (T-

Wound area (%)																
	HGF		*CAL 27*		*SCC-9*		*Detroit 562*		*TR146*		*FaDu*		*Hep-2*		*KB*	
	CTR	*C2*	CTR	*C2*	CTR	*C2*	CTR	*C2*	CTR	*C2*	CTR	*C2*	CTR	*C2*	CTR	*C2*
0h	0	0	0	0	0	0	0	0	0	0	0	0	0	0	0	0
24h	22	15	23	3	61	32	54	15	58	21	43	7	54	3	67	23
48h	65	24	56	4	100	57	100	57	100	50	78	19	95	4	90	46
55h	97	72	83	5	100	91	100	82	100	75	100	32	100	5	100	57

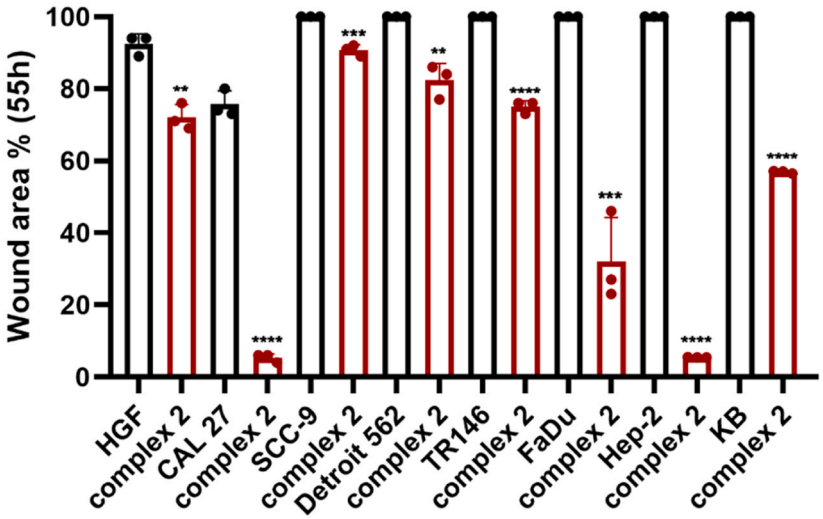

Fig. 7. Graphical representation of comparison of cell migration in cells treated with complex **2** (the concentration corresponded to IC_{25}) and controls (non-treated) after 55 h. Statistical analysis was performed using an unpaired *t*-tests. Results are reported as **p < 0.01, ***p < 0.001, and ****p < 0.0001.

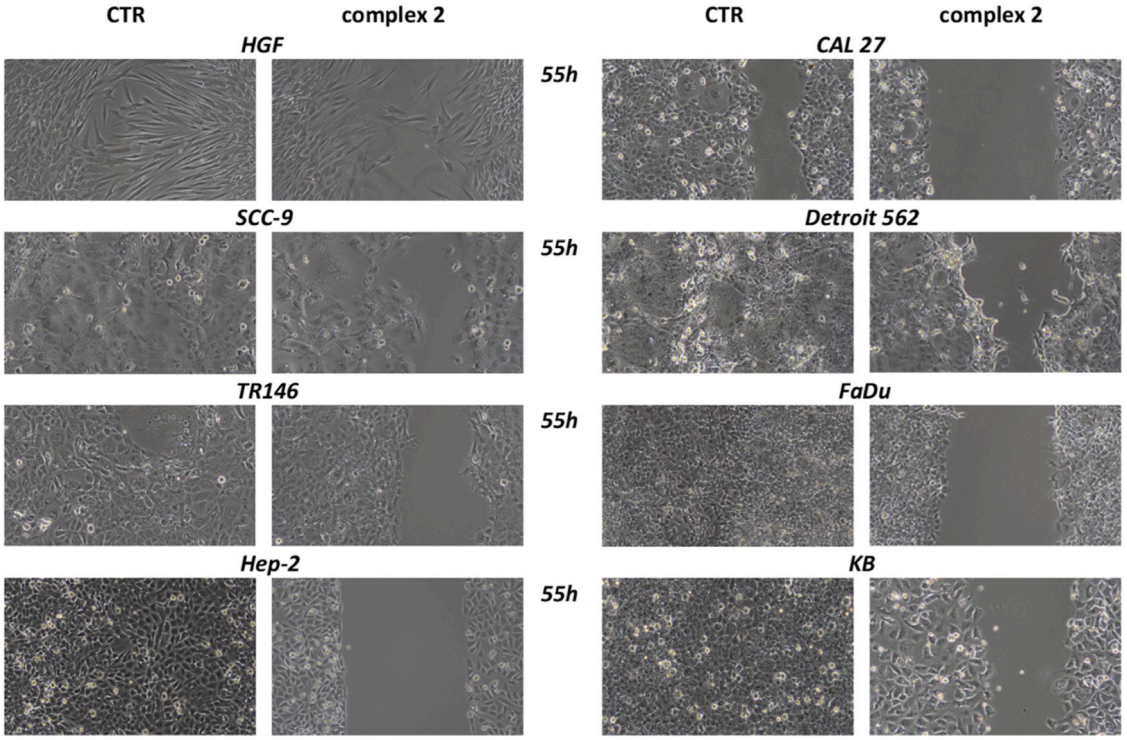

Fig. 8. Microscopic imaging of cell migration and area closure after 55 h. Imaging of complex **2** treated cells (the concentration corresponded to IC_{25}) and control (non-treated).

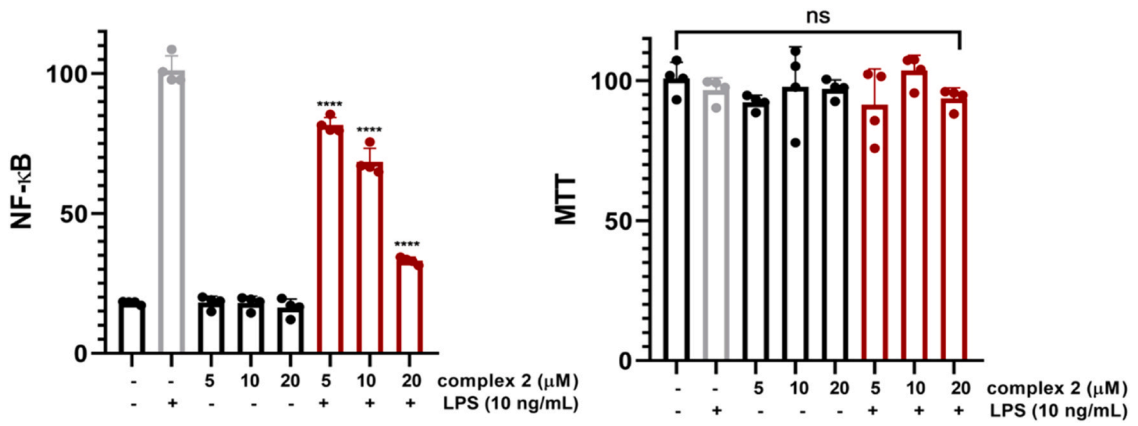

Fig. 9. Inhibition of NF-κB activation using complex **2**. THP1-Blue NF-κB cells were treated with complex **2** (5–20 μM). There is a significant reduction (70 % at a concentration 20 μM) of the NF-κB activation. The MTT viability assay was used to analyze the toxic effect of complex **2** on THP1-Blue NF-κB cells. Data are presented as the mean ± SEM of four independent experiments (n = 4). Statistical analysis was performed using a one-way ANOVA with Dunnett's multiple comparison tests. Results are reported as ns = not significant and ****p < 0.0001.

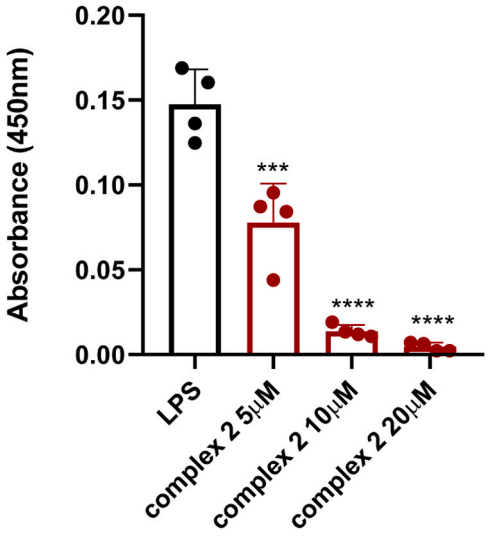

Fig. 10. Detection of NF-κB (p65) to gene promoter after treatment with complex **2** (5–20 μM). Data are presented as the mean ± SEM of four independent experiments (n = 4). Statistical analysis was performed using a one-way ANOVA with Dunnett's multiple comparison tests. Results are reported as ***p < 0.001 and ****p < 0.0001.

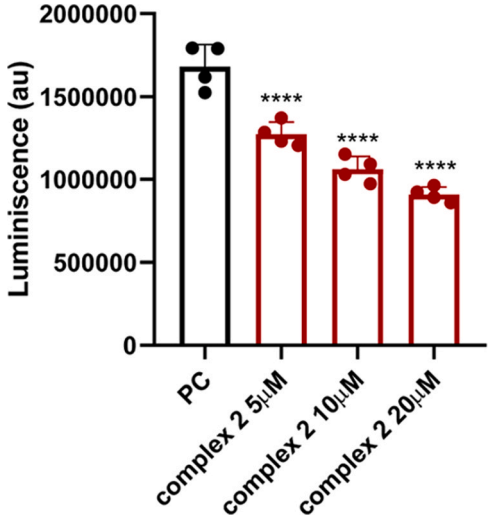

Fig. 11. Detection of IKKβ inhibition after treatment with complex 2 (5–20 μM). Data are presented as the mean ± SEM of four independent experiments (n = 4). Statistical analysis was performed using a one-way ANOVA with Dunnett's multiple comparison tests. Results are reported as ****p < 0.0001.

Jump) defined as fluorescence change induced by sample heating before the thermophoretic molecule transport sets in. T-jump allows the quantification of the affinity of an interaction by changes in the intrinsic temperature dependence of the fluorescence.

A valid MST signal should exhibit an amplitude greater than 5 response units, defined as the difference between the bound and unbound states. We employed the temperature-jump (T-jump) method, which enables quantification of binding affinity by monitoring changes in fluorescence that arise from its intrinsic temperature dependence.

The dissociation constant determined for the interaction between complex **2** and IL-6 was 24.7 ± 15.4 μM, while the interaction with IL-8 yielded a Kd of 11.4 ± 7.1 μM (see Fig. 13). Additionally, the dissociation constant for the interaction of complex **2** with IL-6R was 73.2 ± 43.8 μM (see Figure S8). These results indicate that complex **2** exhibits measurable affinity for IL-6 and IL-8, and a weaker interaction with IL-6R.

4. Discussion

In this study, a new Quinoline-Chalcone-Ruthenium(II) p-Cymene Complex (complex **2**) was synthesized and analyzed. The structure of the resulting complex **2**, a reddish solid, was confirmed by NMR spectroscopy and single-crystal X-ray diffraction. The purity of the material was assessed by NMR and HPLC.

We further studied the effects of complex **2** on selected HNC lines and its anti-inflammatory effects. Complex **2** proved to be relatively cytotoxic against HPV- lines, with significant selectivity against SCC-9 line. Santi et al. tested the Ru(II) complex and found their complex to be toxic against HPV- HNSCC with the highest cytotoxicity against SCC-25, even in 3D cultures [19].

Cell proliferation was tested using CFA treated with complex **2**. Compared to controls, complex **2** suppressed the ability to form colonies. Cells treated with complex **2** formed smaller colonies and less cell colonies. The highest suppression of colony formation occurred after treatment with complex **2** in CAL 27, Detroit 562 and FaDu cells.

Cell migration was monitored using a wound healing assay to evaluate the migration rate in time. Complex **2** reduced or completely

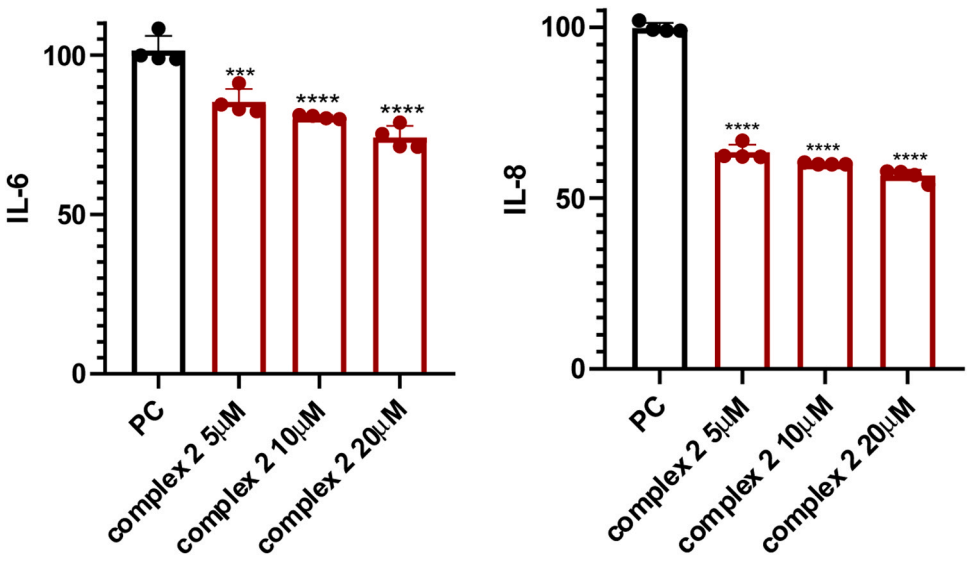

Fig. 12. Sandwich ELISA kit was used to determine the effect of complex **2** on IL-6 and IL-8. The effect of complex **2** was observed at a concentration range 5–20 μM. In both cases, (left) the concentration of IL-6 was reduced after treatment with 20 μM complex **2** (right) the concentration of IL-8 was reduced already after treatment with 5 μM complex **2**. Data are presented as the mean ± SEM of four independent experiments (n = 4). Statistical analysis was performed using a one-way ANOVA with Dunnett's multiple comparison tests. Results are reported as ***$p < 0.001$ and ****$p < 0.0001$.

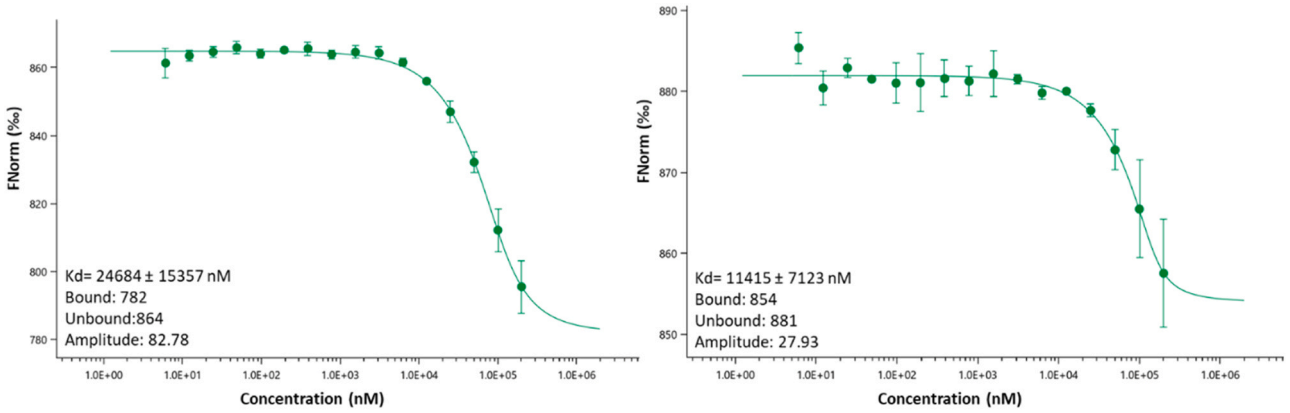

Fig. 13. Binding isotherms for complex **2** with IL-6 (left) and IL-8 (right), obtained by plotting the change in normalized fluorescence as a function of complex **2** concentration.

prevented cell migration. Almost all cell lines showed less than 50 % closure of the formed gap after 55 h, with almost complete growth of the gap compared with the anchorage at 55 h. In HNSCC pathogenesis, metastatic activity is strongly associated with NF-κB activity [44,45].

Increased levels of NF-κB in cancer cells are associated with proliferation, angiogenesis and metastasis. In HNSCC, activation of NF-κB and subsequent increase in pro-angiogenic cytokines such as IL-6 and IL-8 [8,46,47]. Higher IL-6 levels in OSCC patients are associated with an unfavorable prognosis. Wei et al. found that IL-6 is expressed at higher tissue levels in patients with metastatic nodes and relapsed OSCC [48]. In addition, the chemokine IL-8 is also overexpressed in OSCC and is involved in tumor progression and chemoresistance. Overexpression of IL-8 regulates EMT, migration and invasive potential in OSCC cells, thus playing a key role in metastasis. It has also been studied that in OSCC, its targeted blockade may help in the treatment of cisplatin resistance [10].

The synergistic effect of IL-6 and IL-8 regulates the proliferation and migration of tumor cells, including the spread of CTC [49]. These cytokines also regulate positive cell cycle regulators such as NF-κB. It is the inhibition of these cytokines (IL-6 and IL-8) that could improve outcomes including survival in HNSCC patients [10,50].

Jayatilaka et al. found that inhibition of the synergistic IL-6/IL-8 signaling pathway reduced metastatic burden in mice [51]. Furthermore, Yang et al. also found that targeting the IL-6/IL-8 pathway could inhibit metastasis and could lead to increased therapeutic activity, which they observed in a xenograft mouse model [52].

In silico study strongly suggest that complex **2** displays a very strong affinity against NF-κB, IL-8d and especially IL-6d (-12.71 kcal/mol). For compound **1**, which does not contain the Ru(II) ion, the calculated value of binding energy for IL-6d was less significant (-5.71 kcal/mol). Similarly, but smaller difference was obtained for NF-κB and IL-8d. Effect of complex **2** on the NF-κB, IL-8d and IL-6d was also studied by *in vitro*. In the case of NF-κB, a significant suppression of NF-κB activation was observed at a complex **2** concentration of 5 μM. Using 20 μM concentration of complex **2**, NF-κB activation was suppressed by up to 70 %. Furthermore, the effect of complex **2** on IKKβ (an activator of p65) and the affinity of p65 for the corresponding gene promoter was also investigated. Complex **2** exhibited potent inhibitory activity, even at a concentration of 5 μM, reducing IKKβ activity and p65 affinity for the gene promoter by 70 % and 50 %, respectively. At a concentration of 20 μM, IKKβ activity and the amount of p65 bound to DNA were reduced to 50 % and less than 5 %, respectively. These results indicate that complex **2** can effectively interfere with NF-κB signaling through the

inhibition of IKKβ and the reduction of p65's DNA binding ability, likely due to a direct interaction with p65, as predicted by molecular docking studies.

The interaction of complex **2** with IL-6, IL-8, and IL-6R was investigated using both ELISA and microscale thermophoresis (MST). At a concentration of 20 μM, complex **2** resulted in a decrease in the detected protein levels of IL-6 and IL-8 by 30 % and 40 %, respectively. Correspondingly, MST demonstrated a strong affinity of complex **2** for IL-6 and particularly for IL-8, with Kd of 27.4 μM and 11.4 μM, respectively. In contrast, the binding constant for IL-6R was significantly lower (Kd = 73 μM), and the decrease in protein level was not significant, amounting to only 10 %. These results suggest that complex **2** exhibits the most potent effect against NF-κB signaling. While complex **2** can also directly target IL-6 and IL-8, its effect on their protein levels occurs at a significantly slower rate compared to its impact on NF-κB signaling. In the case of IL-6R, potential inhibition cannot be excluded, however, the effective concentration of complex 2 may be too high for effective targeting of IL-6R.

Given the observed inhibitory effects of complex **2** on both proliferative and migratory activity in HNC cell lines future studies should aim to further elucidate its mechanism of action at the molecular level. Detailed pathway analyses, including transcriptomic and proteomic profiling, could confirm the extent of NF-κB, IL-6, and IL-8 axis modulation and identify additional downstream effectors involved.

In the future, it will be necessary to synthesize additional complexes to enable detailed structure–activity relationship studies, which will help optimize the pharmacophoric features of complex **2** and enhance its selectivity and potency. The development of analogues with improved pharmacokinetic and pharmacodynamic properties would represent a critical next step toward preclinical evaluation.

Future plans also include conducting comprehensive pathway analyses, such as transcriptomic and proteomic profiling, which are essential for confirming the extent of NF-κB pathway modulation and identifying additional downstream mediators involved in tumor suppression. Subsequent in vivo experiments in mouse models will also be required.

Overall, these findings support the advancement of complex **2** as a great candidate for further drug development efforts targeting inflammation-driven oncogenesis in head and neck cancers.

5. Conclusion

The newly synthesized ruthenium complex **2** exhibits potent antitumor and anti-inflammatory activity against HNSCC, particularly in HPV-negative cell lines. Its unique molecular architecture—integrating ruthenium, chalcone, and quinoline moieties—represents a rational strategy for designing multifunctional agents capable of targeting key oncogenic and inflammatory pathways. Complex **2** significantly inhibits cell proliferation and migration, effects that appear to be mediated, at least in part, by direct interference with NF-κB, IL-6, and IL-8 signaling. The observed synergistic modulation of IL-6 and IL-8 pathways may contribute not only to cytotoxicity but also to the prevention of tumor progression and metastasis. These findings highlight complex **2** as a promising structural scaffold for the development of novel pharmacophores aimed at improving therapeutic outcomes in HNSCC.

Funding

The author(s) declared that financial support was received for this work and/or its publication. This work was supported by projects of Charles University in Prague (SVV 260755; UNCE/24/MED/022; Progres LF1 Q38 and Q27, Cooperatio Charles University); by the Ministry of Education, Youth, and Sports (Grant No. LM2023053, EATRIS-CZ); by the Technology Agency of the Czech Republic within projects TN02000109 and FW10010306; and by MULTIOMICS_CZ (Programme Johannes Amos Comenius, Ministry of Education, Youth, and Sports of the Czech Republic, ID Project No. CZ.02.01.01/00/23_020/0008540), cofunded by the European Union. The study was also supported by the Ministry of Health, Czech Republic (Grant No. RVO-VFN 64165). We are also grateful for the support of National Institute for Cancer Research and National Institute for the neurological research (Programme EXCELES, ID Project No. LX22NPO5102 and LX22NPO5107, respectively), funded by the European Union, Next Generation EU. The project "Center for Tumor Ecology—Research of the Cancer Microenvironment Supporting Cancer Growth and Spread" (Reg. No. CZ.02.1.01/0.0/0.0/16_019/0000785) is supported by the Operational Programme Research, Development and Education.

CRediT authorship contribution statement

Nikita Abramenko: Formal analysis. **Zdeněk Kejík:** Writing – review & editing, Validation, Methodology. **Ameneh Tatar:** Writing – original draft, Visualization, Conceptualization. **Kateřina Veselá:** Writing – original draft, Methodology, Conceptualization. **Milan Jakubek:** Writing – review & editing, Supervision, Funding acquisition. **Pavel Martásek:** Writing – review & editing. **Petr Babula:** Writing – review & editing. **Michal Masařík:** Writing – review & editing. **Robert Kaplánek:** Formal analysis. **Jan Čejka:** Methodology, Formal analysis.

Declaration of Competing Interest

The authors declare that they have no known competing financial interests or personal relationships that could have appeared to influence the work reported in this paper.

Acknowledgements

We acknowledge CF Diff of CIISB, Instruct-CZ Centre, supported by MEYS CR (LM2023042) and European Regional Development Fund-Project „Innovation of Czech Infrastructure for Integrative Structural Biology" (No. CZ.02.01.01/00/23_015/0008175).

Appendix A. Supporting information

Supplementary data associated with this article can be found in the online version at doi:10.1016/j.biopha.2025.118930.

Data Availability

Data will be made available on request.

References

[1] L.W.J. Baijens, et al., European white paper: oropharyngeal dysphagia in head and neck cancer, Eur. Arch. OtoRhinoLaryngol. 278 (2) (2021) 577–616.
[2] D.E. Johnson, et al., Head and neck squamous cell carcinoma, Nat. Rev. Dis. Prim. 6 (1) (2020) 92.
[3] A. Dittberner, et al., Gender disparities in epidemiology, treatment, and outcome for head and neck cancer in germany: a population-based long-term analysis from 1996 to 2016 of the Thuringian Cancer Registry, Cancers 12 (11) (2020) 3418.
[4] K. Veselá, et al., Curcumin: a potential weapon in the prevention and treatment of head and neck cancer, ACS Pharm. Transl. Sci. 7 (11) (2024) 3394–3418.
[5] C.C. Mireștean, R.I. Iancu, D.P.T. Iancu, p53 modulates radiosensitivity in head and neck cancers—from classic to future horizons, Diagnostics 12 (12) (2022) 3052.
[6] T. de Bakker, et al., Restoring p53 function in head and neck squamous cell carcinoma to improve treatments, Front. Oncol. 11 (2022) 2021.
[7] A. Strzelak, et al., Tobacco smoke induces and alters immune responses in the lung triggering inflammation, allergy, asthma and other lung diseases: a mechanistic review, Int. J. Environ. Res. Public Health 15 (5) (2018) 1033.
[8] S.L. Bhave, T.N. Teknos, Q. Pan, Molecular parameters of head and neck cancer metastasis, Crit. Rev. Eukaryot. Gene Expr. 21 (2) (2011) 143–153.
[9] H.L. Lu, et al., Suppression of phospho-p85α-GTP-Rac1 lipid raft interaction by bichalcone analog attenuates cancer cell invasion, Mol. Carcinog. 55 (12) (2016) 2106–2120.
[10] S. Joshi, et al., Targeted blockade of interleukin-8 negates metastasis and chemoresistance via Akt/Erk-NFκB axis in oral cancer, Cytokine 166 (2023) 156155.

[11] M.J. Clarke, F. Zhu, D.R. Frasca, Non-platinum chemotherapeutic metallopharmaceuticals, Chem. Rev. 99 (9) (1999) 2511–2534.
[12] S. Adhikari, et al., Half-sandwich d 6 metal complexes comprising of 2-substituted-1,8-napthyridine ligands with unexpected bonding modes: synthesis, structural and anti-cancer studies, J. Organomet. Chem. (2017) 854.
[13] J. Pathan, et al., Exploring benzene Ru(II) complexes of 2-subsitituted quinoline/napthyridine ligands: synthesis, biomacromolecular binding and DFT investigations, J. Mol. Struct. 1295 (2024) 136690.
[14] B. Sarkar, et al., Luminescent anticancer ruthenium(ii)-p-cymene complexes of extended imidazophenanthroline ligands: synthesis, structure, reactivity, biomolecular interactions and live cell imaging, Dalton Trans. 48 (32) (2019) 12257–12271.
[15] N. Balakrishnan, et al., Influence of indole-N substitution of thiosemicarbazones in cationic Ru(II)(η6-Benzene) complexes on their anticancer activity, Organometallics 42 (3) (2023) 259–275.
[16] L. Guo, et al., Insights into anticancer activity and mechanism of action of a ruthenium(II) complex in human esophageal squamous carcinoma EC109 cells, Eur. J. Pharmacol. 786 (2016) 60–71.
[17] D. Lovison, et al., Cationic carboxylate and thioacetate ruthenium(ii) complexes: synthesis and cytotoxic activity against anaplastic thyroid cancer cells, Dalton Trans. 49 (24) (2020) 8375–8388.
[18] M. Santi, et al., Hybrid nano-architectures loaded with metal complexes for the co-chemotherapy of head and neck carcinomas, J. Mater. Chem. B 11 (2) (2023) 325–334.
[19] M. Santi, et al., Ruthenium arene complexes in the treatment of 3D models of head and neck squamous cell carcinomas, Eur. J. Med. Chem. 212 (2021) 113143.
[20] M. Brindell, et al., Moving Ru polypyridyl complexes beyond cytotoxic activity towards metastasis inhibition, J. Inorg. Biochem. 226 (2022) 111652.
[21] P. Singh, A. Anand, V. Kumar, Recent developments in biological activities of chalcones: a mini review, Eur. J. Med. Chem. 85 (2014) 758–777.
[22] W. Li, et al., Discovery of novel quinoline-chalcone derivatives as potent antitumor agents with microtubule polymerization inhibitory activity, J. Med. Chem. 62 (2) (2019) 993–1013.
[23] C.-F. Leung, C.-C. Ko, Synthesis and photophysical properties of isocyano Ruthenium(II) quinoline-8-thiolate complexes with visible-light and near-infrared emission, J. Organomet. Chem. 804 (2016) 101–107.
[24] C. Xiong, et al., A bipyridyl quinoline ruthenium(II) complex as a "Light Switch" for living cell mitochondrial singlet oxygen, Sens. Actuators B Chem. 388 (2023) 133868.
[25] X. He, et al., In vitro and in vivo antitumor activity of novel half-sandwich ruthenium complexes containing quinoline derivative ligands, Dalton Trans. 52 (15) (2023) 4728–4736.
[26] M. Kubanik, et al., Impact of the halogen substitution pattern on the biological activity of organoruthenium 8-hydroxyquinoline anticancer agents, Organometallics 34 (23) (2015) 5658–5668.
[27] F.S. Chang, et al., Synthesis and antiproliferative evaluations of certain 2-phenyl-vinylquinoline (2-styrylquinoline) and 2-furanylvinylquinoline derivatives, Bioorg. Med Chem. 18 (1) (2010) 124–133.
[28] W. Cieslik, et al., Contribution to investigation of antimicrobial activity of styrylquinolines, Bioorg. Med Chem. 20 (24) (2012) 6960–6968.
[29] V. Krajka-Kuźniak, M. Belka, K. Papierska, Targeting STAT3 and NF-κB signaling pathways in cancer prevention and treatment: the role of chalcones, Cancers 16 (6) (2024).
[30] H.M. Berman, et al., The protein data bank, Nucleic Acids Res 28 (1) (2000) 235–242.
[31] P. Emsley, et al., Features and development of Coot, Acta Crystallogr D. Biol. Crystallogr 66 (Pt 4) (2010) 486–501.
[32] J. Eberhardt, et al., AutoDock Vina 1.2.0: new docking methods, expanded force field, and python bindings, J. Chem. Inf. Model 61 (8) (2021) 3891–3898.
[33] E.C. Meng, et al., UCSF ChimeraX: tools for structure building and analysis, Protein Sci. 32 (11) (2023) e4792.
[34] E. Krieger, et al., Improving physical realism, stereochemistry, and side-chain accuracy in homology modeling: Four approaches that performed well in CASP8, Proteins 77 (2009) 114–122 (Suppl 9).
[35] The PyMOL Molecular Graphics System, Version 3.0 Schrödinger, LLC.;]. Available from: pymol_0.xml.
[36] Systèmes, D., BIOVIA Workbook. 2024, BIOVIA, Dassault Systèmes.
[37] A. Vangone, et al., Large-scale prediction of binding affinity in protein-small ligand complexes: the PRODIGY-LIG web server, Bioinformatics 35 (9) (2019) 1585–1587.
[38] K. Veselá, et al., Investigating antibacterial and anti-inflammatory properties of synthetic curcuminoids, Front. Med. 11 (2024) **2024**.
[39] A. Altomare, et al., SIR92 - a program for automatic solution of crystal structures by direct methods, J. Appl. Crystallogr. 27 (3) (1994) 435.
[40] P.W. Betteridge, et al., CRYSTALS version 12: software for guided crystal structure analysis, J. Appl. Crystallogr. 36 (6) (2003) 1487.
[41] R.I. Cooper, A.L. Thompson, D.J. Watkin, CRYSTALS enhancements: dealing with hydrogen atoms in refinement, J. Appl. Crystallogr. 43 (2010) 1100–1107, 5 Part 1.
[42] J. Zhang, et al., IκB kinase β (IKKβ): Structure, transduction mechanism, biological function, and discovery of its inhibitors, Int J. Biol. Sci. 19 (13) (2023) 4181–4203.
[43] J.A. Schmid, A. Birbach, IkappaB kinase beta (IKKbeta/IKK2/IKBKB)–a key molecule in signaling to the transcription factor NF-kappaB, Cytokine Growth Factor Rev. 19 (2) (2008) 157–165.
[44] M. Raudenská, J. Balvan, M. Masa, řík, Cell death in head and neck cancer pathogenesis and treatment, Cell Death Dis. 12 (2) (2021) 192.
[45] X. Yang, et al., Head and neck cancers promote an inflammatory transcriptome through coactivation of classic and alternative NF-κB pathways, Cancer Immunol. Res 7 (11) (2019) 1760–1774.
[46] R. Vander Broek, et al., Chemoprevention of head and neck squamous cell carcinoma through inhibition of NF-κB signaling, Oral. Oncol. 50 (10) (2014) 930–941.
[47] D.G. Jackson-Bernitsas, et al., Evidence that TNF-TNFR1-TRADD-TRAF2-RIP-TAK1-IKK pathway mediates constitutive NF-κB activation and proliferation in human head and neck squamous cell carcinoma, Oncogene 26 (10) (2007) 1385–1397.
[48] L.-Y. Wei, et al., Effects of Interleukin-6 on STAT3-regulated signaling in oral cancer and as a prognosticator of patient survival, Oral. Oncol. 124 (2022) 105665.
[49] H. Jayatilaka, J.M. Phillip, Targeting metastasis through the inhibition of Interleukin 6 and 8, Breast Cancer Manag. 8 (1) (2019) BMT20.
[50] E. Ferrari, et al., Salivary cytokines as biomarkers for oral squamous cell carcinoma: a systematic review, Int. J. Mol. Sci. 22 (13) (2021).
[51] H. Jayatilaka, et al., Synergistic IL-6 and IL-8 paracrine signalling pathway infers a strategy to inhibit tumour cell migration, Nat. Commun. 8 (1) (2017) 15584.
[52] H. Yang, et al., Engineered bispecific antibodies targeting the interleukin-6 and -8 receptors potently inhibit cancer cell migration and tumor metastasis, Mol. Ther. 30 (11) (2022) 3430–3449.